



# Toward a Precision Measurement of Binary Black Holes Formation Channels Using Gravitational Waves and Emission Lines

Suvodip Mukherjee<sup>1</sup>  and Azadeh Moradinezhad Dizgah<sup>2</sup> <sup>1</sup> Perimeter Institute for Theoretical Physics, 31 Caroline Street N., Waterloo, Ontario, N2L 2Y5, Canada; [smukherjee1@perimeterinstitute.ca](mailto:smukherjee1@perimeterinstitute.ca)<sup>2</sup> Département de Physique Théorique, Université de Genève, 24 quai Ernest Ansermet, 1211 Genève 4, Switzerland; [Azadeh.MoradinezhadDizgah@unige.ch](mailto:Azadeh.MoradinezhadDizgah@unige.ch)

Received 2022 January 10; revised 2022 September 5; accepted 2022 September 7; published 2022 September 27

## Abstract

The formation of compact objects—neutron stars, black holes, and supermassive black holes—and their connection to the chemical composition of galaxies is one of the central questions in astrophysics. We propose a novel data-driven, multi-messenger technique to address this question by exploiting the inevitable correlation between gravitational waves and atomic/molecular emission-line signals. For a fiducial probability distribution function  $p(t_d) \propto t_d^{-\kappa}$  of time delays, this method can provide a measurement of the minimum delay time of 0.5 Gyr and a power-law index of  $\kappa = 1$  with a standard deviation of 0.12 (and 0.45) and 0.06 (and 0.34), respectively, from five years of LIGO–Virgo–KAGRA observations in synergy with SPHEREx line intensity mapping (and DESI emission-line galaxies). Such measurements will provide data-driven, multi-messenger constraints on the delay time distribution which is currently not well known.

*Unified Astronomy Thesaurus concepts:* [Gravitational waves \(678\)](#); [Black holes \(162\)](#); [Emission line galaxies \(459\)](#)

## 1. Introduction

Gravitational waves (GWs) discovered by the LIGO–Virgo–KAGRA (LVK) scientific collaboration (Acernese et al. 2015; Aasi et al. 2015; Abbott et al. 2016a, 2018; Akutsu et al. 2019, 2021; Acernese et al. 2019) have opened a new window to explore the cosmos using coalescing compact objects such as binary neutron stars (BNSs), binary black holes (BBHs), and neutron star–black hole (NSBH) systems (Abbott et al. 2016b, 2017, 2021b, 2021a, 2021c, 2021d; Abbott et al. 2021). One of the key questions that these measurements can shed light on is the population of binary compact objects and the evolution of their merger rate with cosmic time (Fishbach et al. 2018; Abbott et al. 2019, 2021b, 2021c). The merger rate of BBHs as a function of redshift, inferred until O3 LVK observations, is in agreement with a power-law form  $(1+z)^\gamma$ , with  $\gamma = 2.7^{+1.8}_{-1.7}$  for  $z < 1$  (Abbott et al. 2021c).

The observed population of GW sources can provide insight into how these binary compact objects form in the universe and how their formation relates to the stellar population through the cosmic star formation rate (SFR), stellar mass, and stellar metallicity. While the dependence of the binary merger population on these quantities is not yet known from the data, several simulations have explored the connection between stellar properties and different types of compact objects such as BNSs, NSBHs, and BBHs (Fishbach et al. 2018; Artale et al. 2019, 2020). However, inference of the connection of GW compact objects with host galaxies from observations is challenging due to the large sky localization errors of GW sources.

We propose a novel multi-messenger technique to probe this connection by taking advantage of synergies between atomic and molecular emission lines such as  $H\alpha$ ,  $H\beta$ , [O II], [O III],

[N II], CO, and [C II] as tracers of stellar properties and GW sources such as BNSs, NSBHs, and BBHs as tracers of compact objects. The spectral lines can be detected either in individually resolved galaxies by spectroscopic galaxy surveys probing emission-line galaxies (ELGs) or as aggregate signals using the emerging technique of line intensity mapping (LIM) (Kovetz et al. 2017). In the latter, the spatial fluctuations of the intensity of an emission line together with its frequency provide a three-dimensional map of cosmic large-scale structure. The dependencies of the emission lines and GW sources on stellar populations lead to an inevitable correlation between the two sectors, which depends on the formation channels of GW sources. The luminosity of emission lines determines the amplitude and redshift-dependence of the line power spectrum signal measured by LIM surveys, and the mean number densities of galaxies probed by galaxy surveys. Therefore, the correlation between the observations of GWs and emission lines can provide a model-independent measurement of the dependence of the compact object population on the SFR, stellar mass, and metallicity. Since the proposed method does not rely on the cross-correlation of GW sources with EM probes, the results are not susceptible to the poor sky localization errors of GW sources. For GW sources with very good sky localizations, spatial cross-correlation with EM probes to explore the delay time would provide additional constraining power (Diaz & Mukherjee 2022; Mukherjee et al. 2021; Scelfo et al. 2022).

## 2. Relating GW Sources and Galaxy Properties

Several formation channels for binary compact systems such as BNSs, BBHs, and NSBHs have been proposed in the literature (Banerjee et al. 2010; O’Shaughnessy et al. 2010; Dominik et al. 2012). Different channels lead to different delay time distributions (DTDs)  $P(t_d)$ , which capture the time between the formation of stars and the merging of compact objects. The DTD leaves an imprint on the merger rates of binary systems, their redshift evolution, and their connection



Original content from this work may be used under the terms of the [Creative Commons Attribution 4.0 licence](#). Any further distribution of this work must maintain attribution to the author(s) and the title of the work, journal citation and DOI.

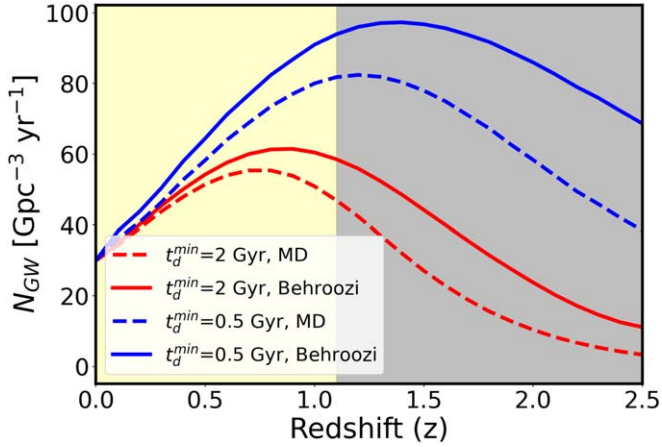


**Figure 1.** The merger rate of GW sources for Madau–Dickinson (MD) and Behroozi models of SFR for two different values of the minimum delay time,  $t_d^{\min} = 0.5$  Gyr and 2 Gyr. The yellow shaded region denotes the maximum redshift range up to which GW sources can be detected by the LVK detectors. The gray-shaded region is accessible by the stochastic GW background.

with their host galaxies. The merger rate of binary compact objects can be written in terms of the DTD  $P(t_d)$  and the SFR density  $R_{\text{SFR}}(z)$  as

$$N_{\text{GW}}(z_m) = \mathcal{N} \int_{z_m}^{\infty} dz \frac{dt_f}{dz} P(t_d) R_{\text{SFR}}(z), \quad (1)$$

where  $\mathcal{N}$  is a normalization constant to set the local merger rate of GW sources with the observed value (Abbott et al. 2021c, 2021d; Virgo & Kagra 2021). The probability distribution of the delay time is expected to follow a power-law form,  $P(t_d) = t_d^{-\kappa}$ , with a value of  $\kappa = 1$  for an initial logarithmic distribution of the separation of the compact objects (McCarthy et al. 2020). Recent works (Toffano et al. 2019; Artale et al. 2020) based on population synthesis simulations combined with galaxy catalogs from hydrodynamical simulations have shown that a different DTD of GW sources can lead to a different dependence of the compact object mergers on the stellar mass ( $M_*$ ), SFR, and stellar metallicity ( $Z$ ) of the host galaxy, which can be expressed by the relation (Artale et al. 2020)

$$\log(n_{\text{GW}}/\text{Gyr}^{-1}) = \gamma_1 \log(M_*/M_{\odot}) + \gamma_2 \log(Z/Z_{\odot}) + \gamma_3 \log(\text{SFR}/M_{\odot}\text{yr}^{-1}) + \gamma_4. \quad (2)$$

Currently, there is no direct measurement confirming this relation from LVK data. Recent studies from individual events (Fishbach & Kalogera 2021) and the stochastic GW background (Mukherjee & Silk 2021) have only been able to put an upper bound on the delay time, assuming a fixed SFR. An upper bound on the stochastic GW background also puts a limit on the high redshift merger rate (Abbott et al. 2021e). The measurement of the DTD will be a direct probe to understand the dependence of binary compact objects on stellar properties. The third-generation GW detectors such as the Cosmic Explorer (CE) (Hall & Evans 2019) and Einstein Telescope (ET) (Punturo et al. 2010; Sathyaprakash et al. 2010), are expected to have sensitivities that can allow inference of the SFR (Vitale et al. 2019) from GW observations. In Figure 1, we show the merger rate of GW sources for two values of the minimum delay time  $t_d^{\min}$  (in red and blue), assuming two SFR models: Madau–Dickinson (Madau & Dickinson 2014)

(dashed) and Behroozi (Behroozi et al. 2013) (solid). A different SFR model results in a variation of the redshift evolution of the merger rate, even if assuming the same form of the DTD.

The DTD for BNSs has been studied in previous works (Safarzadeh & Berger 2019; Safarzadeh et al. 2019; Adhikari et al. 2020). Our focus in this work is on the distribution of delay times for BBHs.

### 3. EM Probes of the Galaxy Properties

In general, the luminosities of emission lines trace star formation and are expected to be correlated with the astrophysical properties of the emitting galaxy. In analogy with Equation (2), this relation can be parameterized as

$$\log(L_{\text{line}}/L_{\odot}) = \alpha_1 \log(M_*/M_{\odot}) + \alpha_2 \log(Z/Z_{\odot}) + \alpha_3 \log(\text{SFR}/M_{\odot}\text{yr}^{-1}) + \alpha_4, \quad (3)$$

where  $\alpha_n$  are the unknown coefficients of the fit, which vary for different lines. For instance, while the [O III], [O II], and [C II] lines are expected to have a strong dependence on metallicity, the H $\alpha$  and H $\beta$  lines should not (Favole et al. 2020; Yang & Lidz 2020).

For the forecast presented in this paper, in the absence of detailed models of line luminosities, as in Equation (3), we use existing scaling relations (Kennicutt 1998; Ly et al. 2007; Silva et al. 2015; Gong et al. 2017) to relate  $L_{\text{line}}$  and SFR, assuming them to depend only on halo mass and redshift. Therefore, SFR ( $M, z$ ) =  $\Gamma_{\text{line}} \times L_{\text{line}}(M, z)$ , with  $\Gamma_{\text{line}}$  being the scaling coefficient for a given line. We use the empirical fit from Behroozi et al. (2013) for SFR( $M, z$ ). To have redshift overlap with LVK observations ( $z \leq 1.1$ ), we consider H $\alpha$  6563 Å, [O III] 5007 Å, and [O II] 3727 Å probed by SPHEREx LIM, and the mean number densities of [O II] ELGs detected by DESI. Following Gong et al. (2017), who took the SFR in units of [ $M_{\odot}\text{yr}^{-1}$ ] and luminosity in units of [ $\text{erg s}^{-1}$ ], we consider  $\Gamma_{\text{line}} = (7.9, 7.6, 14) \times 10^{-42}$  for the H $\alpha$ , [O III], and [O II] lines, respectively.

Given a model of line luminosity, we can compute the mean number density of individually resolved line emitters,  $\bar{n}(z) = \int_{M_{\min}}^{M_{\max}} dM n(M, z)$ , by matching the minimum mass ( $M_{\min}$ ) of halos hosting line-luminous galaxies to the minimum luminosity ( $L_{\min}$ ) detectable by a given galaxy survey. Considering the [O II] galaxies observed by the upcoming DESI survey, we set  $\log_{10}(L_{\min}/\text{erg s}^{-1}) = (40.5, 41)$  for redshift ranges of  $0.65 \leq z < 1$  and  $1 \leq z \leq 1.65$ , which are in broad in agreement with values presented by Comparat et al. (2016) and Saito et al. (2020).

For the LIM, we are interested in the statistical properties of the fluctuations of line intensities. We summarize the key quantities here, and refer the reader to Gong et al. (2020) and Moradinezhad Dizgah et al. (2022) for further details. Using the halo-model framework, the mean intensity of a line (in units of [Jys/sr]) is related to the dark matter (DM) halo properties as

$$\bar{I}_{\text{line}}(z) = \int_{M_{\min}}^{M_{\max}} dM n(M, z) \frac{L_{\text{line}}(M, z)}{4\pi \mathcal{D}_L^2(z)} \left( \frac{dl}{d\theta} \right)^2 \frac{dl}{dv}, \quad (4)$$

where  $n(M, z)$  is the halo-mass function,  $\mathcal{D}_L$  is the luminosity distance, and  $(dl/d\theta)^2 dl/dv$  reflects the conversion from comoving volume to observed specific intensity volume

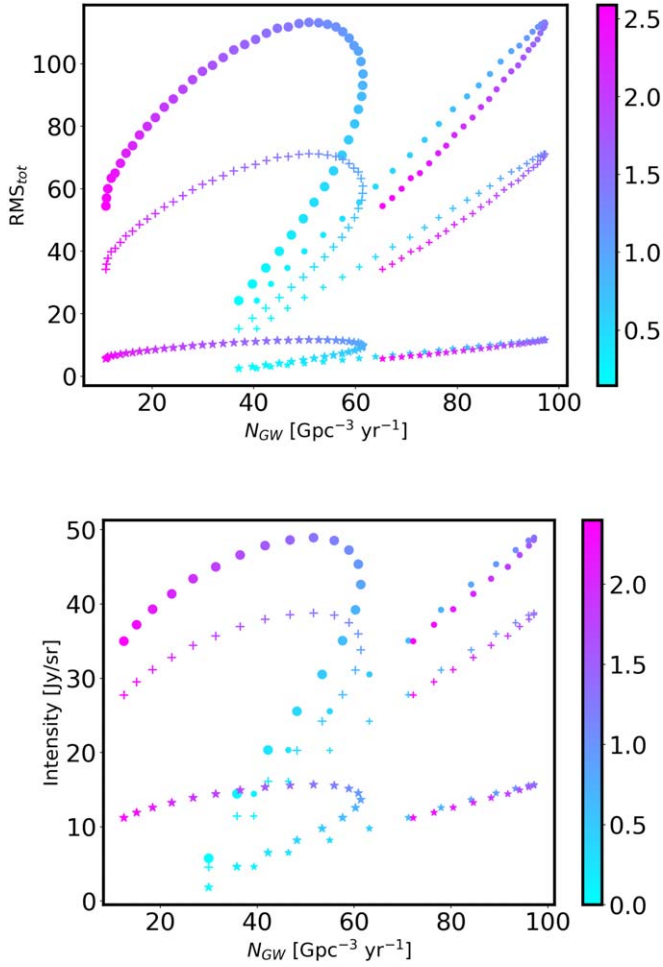


**Figure 2.** The correlations between GW sources,  $N_{\text{GW}}$ , and the rms signal of LIM (top panel) and the ELG intensity (bottom panel) as a function of cosmological redshift (shown by the color bar). Different marker styles correspond to the  $\text{H}\alpha$  (circles),  $[\text{O III}]$  (crosses), and  $[\text{O II}]$  (stars) lines. The large and small markers show the correlations for two different DTDs of  $t_d^{\text{min}} = 0.5$  Gyr (small markers) and  $t_d^{\text{min}} = 2$  Gyr (large markers).

defined in terms frequency,  $\nu$ , and angular size,  $\theta$ . On large scales, line intensity fluctuations can be described as a linearly biased tracer of the underlying DM distribution,  $\delta_{\text{line}}(\mathbf{k}, z) = \bar{I}_{\text{line}}(z)b_{\text{line}}(z)\delta_m(\mathbf{k}, z)$ . Therefore, in the absence of anisotropies, the clustering component of the line intensity power spectrum (in units of  $[(\text{Jy}/\text{sr})^2(\text{Mpc}/h)^3]$ ) is given by

$$P_{\text{LIM}}^{\text{clust}}(k, z) = [\bar{I}_{\text{line}}(z)b_{\text{line}}(z)]^2 P_m(k, z). \quad (5)$$

Additionally, the observed line power spectrum includes a shot-noise contribution due to the discreteness of line-emitting galaxies and the thermal noise of the instrument. In the Poisson limit, the former is given by

$$P_{\text{LIM}}^{\text{shot}}(z) = \int_{M_{\text{min}}}^{M_{\text{max}}} dM n(M, z) \left[ \frac{L_{\text{line}}(M, z)}{4\pi D_L^2(z)} \left( \frac{dl}{d\theta} \right)^2 \frac{dl}{d\nu} \right]^2. \quad (6)$$

The model of the power spectrum used in our forecasts further includes redshift-space distortions, the Alcock–Paczynski effect, and interloper lines (Cheng et al. 2016; Lidz & Taylor 2016).

#### 4. Expected Correlation between the GW Signal and the Emission-line Signal

As discussed in Section 2 (Equation (2)), using numerical simulations, previous studies (Artale et al. 2019, 2020) have shown that the expected merger rates of GW sources strongly depend on the SFR, stellar mass, and metallicity. As a result, depending on the local behavior of these quantities, we can write Equation (2) in terms of a matrix<sup>3</sup>

$$\mathbf{N}(z) = \mathbf{G}(z)\mathbf{S}(z), \quad (7)$$

where  $\mathbf{N}(z) = [n_{\text{BNS}}(z), n_{\text{NSBH}}(z), n_{\text{BBH}}(z)]$  refers to the number density of GW sources of the three binary types and  $\mathbf{G}$  is a matrix of the coefficients of the relation between the number densities of GW sources and the astrophysical properties of the galaxies, represented by  $\mathbf{S}(z)$ . The DTD of compact objects controls the values of the elements of matrix  $\mathbf{G}$  and it depends on the stellar properties of the host galaxy. Previous analyses by Artale et al. (2019, 2020) have shown the behavior of this scaling relation across a wide redshift range of  $z \in [0, 6]$ . In Equation (7), the connection between the GW merger rate to Population III stars is not included and modification to this expression will be required.

In constructing Equation (7), two major assumptions enter. First, it depends on the theoretical modeling of the stellar properties and formation channel scenario, and this relation is not yet constrained by data. Second, it is written in terms of average galaxy properties at every redshift. As different galaxies at each redshift will exhibit a variation from the global average, this relation will show variations. Due to the large sky localization errors of GW sources, we cannot uniquely identify the host galaxy unless there is an EM counterpart. In this work, we propose a way to evade the first problem and partly solve the second problem by using a multi-messenger approach. In the following discussion we show that by exploring a direct relation of the GW merger rate with the signal from ELGs and LIM, we can probe their dependencies on the formation channel. Furthermore, the proposed technique makes it possible to consider the halo-mass-dependent SFR and also explore the dependences on metallicity and stellar mass. Therefore, we can investigate the dependence of the merger rates on different galaxy properties. In this analysis, we focus on GW sources without EM counterparts. For sources with an EM counterpart, this approach can be even more powerful.

A promising observational probe of the stellar properties of galaxies are the resolved emission-line galaxies and the aggregate intensity mapping signal of spectral emission lines. The amplitudes of both signals are determined by the specific luminosity of the spectral line of interest, given in Equation (3). This relation can be cast in matrix form as

$$\mathbf{E}(z) = \mathbf{A}(z)\mathbf{S}(z), \quad (8)$$

where  $\mathbf{E}(z)$  can be the intensity of the ELGs or rms fluctuation of the LIM signal for different lines and  $\mathbf{A}$  is a matrix whose coefficients relate to the observed strength of the emission-line signal with the global astrophysical properties, represented by  $\mathbf{S}$ . Since GW sources, their merger rates, and the line emission depend physically on the same astrophysical quantities, we can

<sup>3</sup> Bold fonts denote matrices.

combine Equations (7) and (8) as

$$N(z) = \mathbf{G}(z)\mathbf{A}^{-1}(z)\mathbf{E}(z) \equiv \mathbf{K}(z)\mathbf{E}(z), \quad (9)$$

where  $\mathbf{K}(z) \equiv \mathbf{G}(z)\mathbf{A}^{-1}(z)$  denotes a matrix whose coefficients capture the connection between the GW source properties and the emission-line signal. In the above equation,  $N(z)$  and  $E(z)$  can be measured from GW and EM observations, respectively. Although the connection matrices  $\mathbf{G}$  and  $\mathbf{A}$  are not well known, we can infer matrix  $\mathbf{K}$  by combining the two independent observations, without invoking any model. The values of the elements of matrix  $\mathbf{K}$  depend on the formation channel, which is now encapsulated in terms of observable probes, such as ELGs and LIM signals as a function of redshift. The redshift evolution of the elements in matrix  $\mathbf{K}$  is controlled by the DTD. As we will show below, for scenarios with a large delay time, the merger rate of compact objects will show a strong correlation with lower SFRs at lower redshifts. In comparison, if the delay time is small, then the higher merger rate of compact objects will exhibit stronger correlations with galaxies having large star formation activities. By measuring the value of  $\mathbf{K}$  as a function of redshift from a combination of GWs and emission-line data, we can reconstruct the DTD. The tomographic measurement of the correlation with redshift makes it possible to reconstruct the DTD.

Using a generative model of GW merger rates for two scenarios of the DTD and an SFR model that captures the halo-mass dependence, in Figure 2, we show how the correlation between the GW merger rate and ELG (and LIM) signals of different spectral lines can vary when changing the DTD. More specifically, we assume the SFR of Behroozi et al. (2013) and a DTD of the form  $P(t_d) \propto t_d^{-\kappa}$  with two different values of the minimum delay time parameter of  $t_d^{\min} = 0.5$  Gyr and 2 Gyr (shown in small- and large-size markers, respectively). The upper panel shows the correlation between  $N_{\text{GW}}$  and the rms fluctuations of the LIM signal, while the lower panel shows the correlation with the mean intensity of ELGs. The three curves from top to bottom in each panel, shown by circles, crosses, and stars, correspond to the  $\text{H}\alpha$ ,  $[\text{O III}]$ , and  $[\text{O II}]$  lines, respectively. This plot indicates that the trajectory of the correlation between the emission lines and GW sources shows different behavior for different delay time scenarios. If the delay time is small, then the GW sources will exhibit a longer correlation with the emission-line signals before turnover, in comparison to the case of a large delay time. Moreover, depending on whether the strengths of the emission lines signals strongly correlate at all redshifts, the correlation will show a positive helicity, in comparison to a negative helicity when the GW sources will not follow the emission-line signals up to a high redshift. It is noteworthy that GW sources of different masses can exhibit slightly different dependences on the delay time, and hence a different dependence on the emission-line signals. The probability distribution  $P(t_d, \mathcal{M}) = t_d^{-\kappa(\mathcal{M})}$  with the minimum delay time can have a mass dependence of  $t_d^{\min}(\mathcal{M})$ . Therefore, the mass dependence of the delay time can also be captured using the method presented here.

It should be noted that the redshift uncertainties in the measurements of  $N(z)$  and  $E(z)$  set the accuracy with which the redshift-dependence of  $\mathbf{K}(z)$ , which carries information about the formation channels of the binary compact objects, can be

determined. The redshift uncertainty of the EM measurement and the luminosity distance uncertainty in the GW signal can be incorporated in the above equation with a window function,  $W(z, z')$  and  $D(\mathcal{D}_L, z)$ , which modifies Equation (9) to

$$N(z) \equiv D(\mathcal{D}_L, z)N(\mathcal{D}_L) = \mathbf{K}(z)\mathbf{W}(z, z')\mathbf{E}(z'). \quad (10)$$

## 5. Fisher Forecasts

As described in the previous section, the merger rate of GW sources and the number density of ELGs or the amplitude of the LIM power spectrum can exhibit a correlation due to the dependence of both signals on the underlying stellar properties of the galaxies, such as stellar mass, SFR, and stellar metallicity. By comparing the observed redshift distribution of the ELG (or LIM) signal with the observed merger rate of the GW sources, this correlation can be measured. In this section, we apply this idea to mock BBH samples and ELG/LIM signals generated assuming an underlying model of the SFR and DTD for three different emission lines, namely  $\text{H}\alpha$ ,  $\text{O [II]}$ , and  $\text{O [III]}$ . So in Equation (9), matrix  $\mathbf{K}$  becomes a row matrix with dimensions of  $1 \times 3$  and matrix  $\mathbf{E}$  becomes a column matrix with dimensions of  $3 \times 1$  which need to be computed as a function of redshift to make a tomographic estimation. By performing a Fisher matrix analysis, we show that the achievable constraints on the DTD from current surveys such as LIGO (Aasi et al. 2015; Abbott et al. 2016a), Virgo (Acernese et al. 2015, 2019), and KAGRA (Abbott et al. 2018; Akutsu et al. 2019, 2021) are in synergy with near-term LIM surveys such as SPHEREx and ELGs from DESI.

As described earlier, we consider the Behroozi et al. (2013) SFR to generate the ELG signal as a function of redshift, which is detectable by DESI using the equation

$$\bar{n}(z) = \int_{M_{\min}}^{M_{\max}} dM n(M, z), \quad (11)$$

where  $M_{\min}$  corresponds to the halo mass for the minimum luminosity detectable by surveys like DESI. For an LIM signal, assuming the same SFR model, we compute the power spectrum of line intensity fluctuations (given by Equations (5) and (6)), and calculate the total rms fluctuations given by

$$\sigma_\ell^2(z) = \sum_i^{k_{\max}} k_i^2 \Delta k / (2\pi)^2 W^2(R_s, k_i) P_\ell(k_i, z). \quad (12)$$

Here,  $P_\ell(k, z) \equiv (2\ell + 1)/2 \int_{-1}^1 d\mu P(k, \mu; z) \mathcal{L}_\ell(\mu)$ , where  $\mu$  is the angle with respect to line-of-sight direction,  $\mathcal{L}_\ell$  are the Legendre polynomials (with  $\ell = 0, 2, 4$ ), and  $P(k, \mu; z)$  is the anisotropic power spectrum. In the summation,  $k_i$  is the wavenumber at the center of the  $i^{\text{th}}$   $k$ -bin of width  $\Delta k$  (set to be the fundamental mode of the survey),  $k_{\max} = 0.3 h \text{ Mpc}^{-1}$ , and  $W(R_s, k)$  is a top-hat smoothing kernel in real space with  $R_s = 8 \text{ Mpc } h^{-1}$ . For LIM surveys, the redshift uncertainty,  $\sigma_z = (1 + z)/\mathcal{R}$ , is determined by the resolution of the instrument denoted by  $\mathcal{R} \equiv \nu/\Delta\nu$ , while for DESI, we assume  $\sigma_z = 0.001(1 + z)$ .

For generating the GW sources, we consider the same Behroozi et al. (2013) SFR and consider a power-law model of the DTD,  $P(t_d) \propto t_d^{-\kappa}$ , assuming three different scenarios with (i)  $\kappa = 1$  and a minimum DTD of  $t_d^{\min} = 0.5$  Gyr, (ii)  $\kappa = 1$  and

$t_d^{\min} = 2.0$  Gyr, and (iii)  $\kappa = 1.2$  and  $t_d^{\min} = 0.5$  Gyr. For each of these scenarios, we generate a mock sample of GW sources with a redshift distribution using Equation (1). We consider a power-law mass distribution of BBHs with ( $m^{-2.35}$ ) for the heavier objects and  $m^{-1}$  for the lighter ones, motivated by the recent measurements of Abbott et al. (2021b, 2021c). We estimate the matched filtering signal-to-noise ratio (S/N),  $\rho$ , for binary systems with a detector-frame chirp mass of  $\mathcal{M}_d$  at a luminosity distance of  $\mathcal{D}_L$ , using the relation (Farr et al. 2016; Mastrogiovanni et al. 2021)

$$\rho = \rho_* \Theta \left( \frac{\mathcal{M}}{\mathcal{M}_d^*} \right)^{5/6} \left( \frac{\mathcal{D}_L^*}{\mathcal{D}_L} \right), \quad (13)$$

where  $\Theta$  is the detector projection factor assumed to be uniform between  $[0, 1]$ . The parameters  $\mathcal{D}_L^*$  and  $\mathcal{M}_d^*$  are the reference chirp mass and luminosity distance, respectively, at which an optimally oriented binary has an S/N of  $\rho_* = 8$ . For our mock data, we set the values of  $\mathcal{M}_d^* = 26.12 M_\odot$  and  $\mathcal{D}_L^* = 2.5$  Gpc,  $\mathcal{D}_L^* = 2.1$  Gpc, and  $\mathcal{D}_L^* = 1.2$  Gpc for aLIGO, Virgo, and KAGRA, respectively, according to Abbott et al. (2018). The combined matched filtering S/N for the network of detectors is obtained by using  $\rho_{\text{det}}^2 = \sum_i \rho_i^2$ , and we select samples with  $\rho_{\text{det}} \geq 10$ . We draw posterior samples of the GW source parameters by using the approximate form of the likelihood for the chirp mass and mass ratio given by Farr et al. (2016) and Mastrogiovanni et al. (2021). We estimate the posterior distribution of the luminosity distance using a Gaussian approximation. Though the results from individual events are likely to be non-Gaussian, the results after combining several events are expected not to vary significantly due to the approximation of the Gaussian posterior by the central limit theorem. Therefore, the Fisher forecasts presented in this paper will not be significantly affected by this assumption. The detection of the GW sources of lighter mass sources situated at higher luminosity distances with  $\rho_{\text{det}} \geq 10$  is rare. As a result, an appropriate selection function depending on the source properties also needs to be taken into account.

For the mock samples of GW sources and ELG/LIM signals from the same generative model of the SFR, using Equation (9), we can now infer the values of the elements of matrix  $\mathbf{K}$  for different emission lines as a function of redshift. In this process, for each independent emission line, we find the values of the coefficients  $K_{[\text{GW}][\text{ELG/LIM}]}$  at every redshift using the computed  $N_{\text{GW}}(z)$  and ELG/LIM signals. We compute the coefficients for all the three lines considered here and obtain matrix  $\mathbf{K}$  at each redshift with an overall normalization factor that is matched with the total number of observed GW sources. The total number of GW sources cannot be constrained using this formalism (as it is absorbed in the overall normalization), but we can constrain the redshift evolution of the coefficients of the matrix elements, which is useful in measuring the DTD. The values of individual coefficients are shown in Figure 3, where we can see that for different DTDs, the elements of matrix  $\mathbf{K}$  evolve differently with redshift. As we consider only BBHs in this analysis, the corresponding matrix element for BBHs is shown as a function of redshift for three different emission lines, H $\alpha$ , O[II], and O[III]. The overall amplitude of the distribution depends on the total number of GW sources, and its evolution with redshift is driven by the nature of the

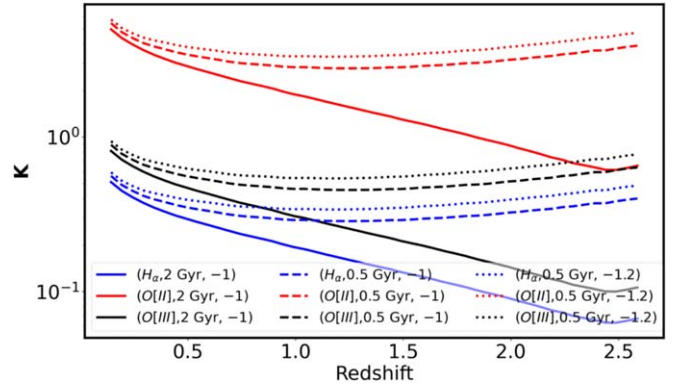


**Figure 3.** The values of elements of matrix  $\mathbf{K}$  for BBHs as a function of redshift for different lines and for three different cases of the DTD, as indicated in the label in the following order (emission line, minimum delay time, and power-law index).

DTD. The correlation coefficients are larger for the O[II] and O [III] lines compared to the H $\alpha$  line. The nature of the redshift evolution of the values of the coefficients in matrix  $\mathbf{K}$  is related to the correlation plot shown in Figure 2. The corresponding physical explanation of this redshift evolution is discussed in Section 4. For small (or large) values of the minimum delay time and a steeper (or shallower) power-law index of the DTD, the mergers of BBHs shift toward a higher (or lower) redshift. As a result, the values in matrix  $\mathbf{K}$  will show a stronger correlation with the ELG/LIM signal for the former case than in the latter case. The similarity in the behavior of the values of the elements in matrix  $\mathbf{K}$  for different lines is because the same SFR model regulates the ELG/LIM signal and for the same SFR, the GW source distribution changes for different DTDs as a function of redshift. As the same underlying SFR contributes to both the ELG/LIM signal for different emission lines and GW sources, it becomes possible to infer the DTD from the GW sources by jointly using both GW data and ELG/LIM data, which helps in mitigating the uncertainty associated with the SFR. For models of the DTD that differ from a power-law model, the values of the elements in matrix  $\mathbf{K}$  will show different behavior. Let us note that the DTD can also depend on the source properties of the GW events such as their masses, spin, etc. We leave the investigation of how the proposed technique can be used to explore this aspect for future work.

With the above ingredients, we perform a Fisher analysis to estimate how well the DTD parameters can be measured using the correlations of the GW and EM signals. The Fisher matrix  $\left( F_{\alpha\beta} \equiv \left\langle \frac{\partial^2 \mathcal{L}}{\partial \theta_\alpha \partial \theta_\beta} \right\rangle \right)$  can be written in terms of the log-likelihood ( $\mathcal{L} = -\ln(L)$ ) for the parameters  $\theta \in \{t_d^{\min}, \kappa\}$

$$\begin{aligned} 2\mathcal{L}(\theta) &= \sum_{L_i} \sum_{z_k} \sum_{\mathcal{M}_*} \frac{(\hat{N}_{\text{GW}}(z_k, \mathcal{M}_*) - K(z_k, \mathcal{M}_*, \theta)E(z, L_i))^2}{C(z_k, \mathcal{M}_*, L_i)} \\ &+ \text{Indet}(C(z_k, \mathcal{M}_*, L_i)), \end{aligned} \quad (14)$$

and the standard deviation (Cramer–Rao bound) on parameter  $\theta_\alpha$ , denoted by  $\Sigma_\alpha$ , can be obtained by taking the square root of the  $\alpha$  component of the inverse of the Fisher matrix  $\Sigma_\alpha = \sqrt{(\mathbf{F}^{-1})_{\alpha\alpha}}$ . In Equation (14),  $\hat{N}_{\text{GW}}(z_k, \mathcal{M}_*)$  is the observed number of GW sources at redshift  $z_k$  and mass-bin centered at  $\mathcal{M}_*$ , while

$K(z_k, M_*)E(z, L_i)$  denotes the theoretical prediction for the number of GW sources,  $N_{GW}$ , for a given emission-line signal and different parameters related to the delay time. In the denominator,  $C(z_k, M_*, L_i) = \sigma_p^2 + \sigma_e^2 + \sigma_r^2$  denotes the covariance matrix, which we assume to be diagonal and consisting of three parts, namely  $\sigma_p^2 = N_{GW}$ , which is the Poisson error on the GW source number,  $\sigma_e^2 = (\partial N_{GW} / \partial L_i)^2 \sigma_{L_i}^2$ , which is the error in the GW numbers due to a change in the luminosity of the  $i^{th}$  emission line,  $\sigma_r^2 = (\partial N_{GW} / \partial z)^2 [(\partial z / \partial D_L)^2 |_{\Theta_c} \sigma_{D_L}^2 + \sigma_z^2]$  is the error in the redshift due to the error in the luminosity distance measurement  $\sigma_{D_L}^2$  for the fixed cosmological parameters denoted by  $\Theta_c$  (set to Planck values from Aghanim et al. 2020), and  $\sigma_z^2$  is the redshift uncertainty in the EM sector. The major sources of uncertainty are the luminosity distance and the Poisson errors on the GW sources. The additional uncertainty due to the stochasticity of the DTD specific to the sources is subdominant due to the all-sky averaging of the LIM signal and a large number of ELGs. The elements of the Fisher matrix are calculated by taking the numerical derivative of the matrix elements of  $K$  with changes in the DTD parameters  $\theta$  as  $\partial K(z_k, M_*, \theta) / \partial \theta_\alpha = \frac{1}{\Delta \theta_\alpha} [K(z_k, M_*, \theta_\alpha + \Delta \theta_\alpha / 2) - K(z_k, M_*, \theta_\alpha - \Delta \theta_\alpha / 2)]$ .

For the LIM, we consider the redshift range of  $z_{\max} = 1.1$  and  $z_{\min} = \{0.2, 0.5, 1.0\}$  for the H $\alpha$ , [O III], and [O II] lines, which can be probed in the lowest frequency band of SPHEREx with a spectral resolution of  $\mathcal{R} = 41$ , and over two 100 deg<sup>2</sup> fields (Doré et al. 2014). The instrument noise  $P_N(z) = V_{\text{vox}} \sigma_{I, \text{vox}}^2$  depends on the voxel comoving volume  $V_{\text{vox}}$  and the voxel intensity noise  $\sigma_{I, \text{vox}}$ . Furthermore, we account for signal attenuation due to the Fourier spectral and angular point-spread functions, which render the instrument noise scale-dependent. We account for contamination from both foreground and background line interlopers. For DESI, we consider the mean number density of the [O II] emitters at  $0.65 \leq z \leq 1.1$ .

In Figure 4, we show the 2D marginalized constraints on the parameters  $t_d^{\min} = 0.5$  Gyr and  $\kappa = 1$  from a combination of GW and LIM data from SPHEREx and the mean number densities of ELGs from DESI using the Fisher formalism. The plots indicate that we can measure the delay time parameter and the fiducial model of the power-law index of the probability distribution function with corresponding error bars of  $\Sigma_{t_d^{\min}} = 0.12$  (and 0.18) and  $\Sigma_\kappa \sim 0.06$  (and 0.095) for 5 yr (and 2 yr) of observation from LVK in synergy with SPHEREx. Using DESI, the precision on the parameters degrades by about a factor of 3.5 due to the limited availability of ELGs at lower redshift, and also for having only [O II] emission-line signal. This shows that the first precise measurement of the DTD will be possible in the near future with LVK. For comparison, an upper bound on the DTD available from the first half of the third observation run is  $t_d^{\min} < 2.2$  Gyr (Fishbach & Kalogera 2021), assuming a fixed value of the power-law index of  $\kappa = 1$  and for a fixed SFR (Madau & Fragos 2017). The technique we propose does not require an assumption on the form of the SFR, while it allows us to explore the DTD and its correlation with stellar metallicity using a multi-messenger avenue. By considering different SFR model parameters (with a general form given by the Madau–Dickinson model) when generating the mock data, we have found that the constraining power of the DTD by this technique

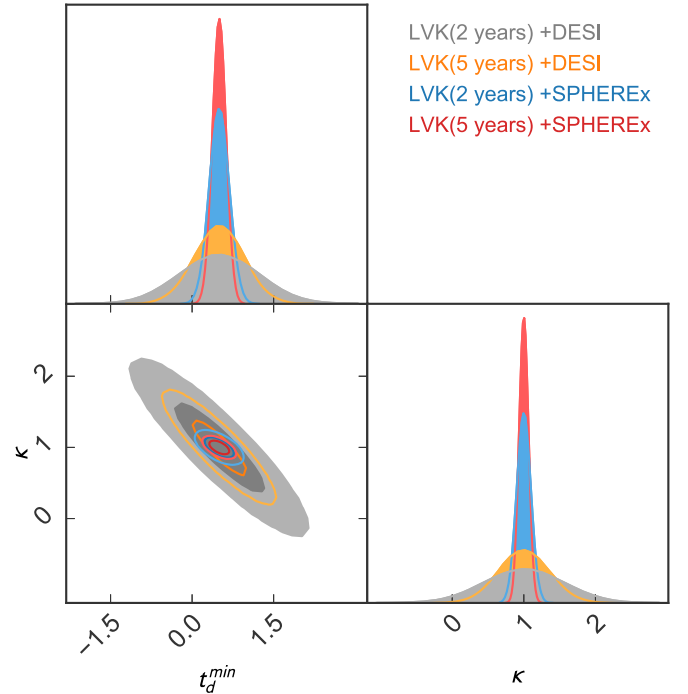


**Figure 4.** Fisher forecast for measuring the minimum delay time  $t_d^{\min} = 0.5$  Gyr and power-law index  $\kappa$  of the probability distribution  $P(t_d) = t_d^{-\kappa}$  using LVK data and the emission-line signals from LIM by combining the H $\alpha$ , [O III], and [O II] lines from SPHEREx (blue and red), and [O II] ELGs from DESI (gray and yellow). The current constraint on the delay time  $t_d^{\min}$  is  $< 2.2$  Gyr at a 90% credible interval assuming a fixed SFR and  $\kappa = 1$  obtained from the individual events detected in the first half of the third observation run.

is possible for a wide range of SFR parameters. The model parameters which control the peak of the SFR history and the slope at low redshifts have a maximum impact on the GW merger rates accessible by LVK.

## 6. Conclusions and Future Prospects

In this letter, we introduced a novel multi-messenger avenue to explore the formation channel of compact objects by studying the correlation between different emission-line signals from ELGs or LIM. We showed that the network of LVK detectors, in conjunction with the LIM signals of H $\alpha$  and [O III] lines measured by SPHEREx or the number count of ELGs detectable by DESI, can constrain the minimum delay time value and the power-law index of the probability distribution with decent precision. The proposed method can equally be applied to understand the dependence of the compact objects on SFR and metallicity, not only for stellar-mass black holes, but also for the BNSs, NSBHs, and also for SMBHs. The connection between BNSs, NSBHs, and SMBHs will be possible to explore from the next generation GW detectors such as CE, ET, and LISA in synergy with multiline LIM signals and ELGs.



This is the first work showing the potential of this multi-messenger approach to probe the DTD of BBHs. There are several directions in which this work can be extended. This technique can further shed light on the formation channel of BBHs and can also distinguish primordial black hole populations. Moreover, in this current work, we have assumed a fixed value of the cosmological parameters to relate the observed GW sources with emission lines. Joint estimation of the cosmological parameters and the delay time parameter is also

possible by this technique. In summary, the combined study of the emission lines and GW sources can play a crucial role in exploring several new territories in astrophysics and fundamental physics.

The authors are thankful to Maya Fishbach for reviewing this manuscript as a part of the LVK publication and presentation policy and for providing useful comments. The authors would like to thank Olivier Doré, Garrett K. Keating, and Pascal Oesch for their valuable input. S.M. is supported by the Simons Foundation. Research at Perimeter Institute is supported in part by the Government of Canada through the Department of Innovation, Science and Economic Development and by the Province of Ontario through the Ministry of Colleges and Universities. A.M.D. is supported by the SNSF project “The Non-Gaussian Universe and Cosmological Symmetries”, project No.:200020-178787. A.M.D. also acknowledges partial support from Tomalla Foundation for Gravity. The authors would like to thank the LIGO/Virgo scientific collaboration for providing the noise curves. LIGO is funded by the U.S. National Science Foundation. Virgo is funded by the French Centre National de Recherche Scientifique (CNRS), the Italian Istituto Nazionale della Fisica Nucleare (INFN), and the Dutch Nikhef, with contributions by Polish and Hungarian institutes. This material is based upon work supported by NSF’s LIGO Laboratory which is a major facility fully funded by the National Science Foundation.

*Software:* Astropy (Astropy Collaboration et al. 2013), matplotlib (Hunter 2007), NumPy (van der Walt et al. 2011), SciPy (Jones et al. 2001), pygtd (Bocquet & Carter 2016).

### ORCID iDs

Suvodip Mukherjee  <https://orcid.org/0000-0002-3373-5236>  
Azadeh Moradinezhad Dizgah  <https://orcid.org/0000-0001-8841-9989>

### References

Aasi, J., Abbott, B. P., Abbott, R., et al. 2015, *CQGra*, 32, 074001  
Abbott, B. P., Abbott, R., Abbott, T. D., et al. 2016b, *PhRvL*, 116, 061102  
Abbott, B. P., Abbott, R., Abbott, T. D., et al. 2016a, *PhRvD*, 93, 112004  
Abbott, B. P., Abbott, R., Abbott, T. D., et al. 2017, *PhRvL*, 119, 161101  
Abbott, B. P., Abbott, R., Abbott, T. D., et al. 2018, *LRR*, 21, 3  
Abbott, B., Abbott, R., Abbott, T. D., et al. 2019, *ApJL*, 882, L24  
Abbott, R., Abbott, T., Abraham, S., et al. 2021a, *PhRvX*, 11, 021053  
Abbott, R., Abbott, T. D., Abraham, S., et al. 2021b, *ApJL*, 913, L7  
Abbott, R., Abbott, T. D., Acernese, F., et al. 2021c, arXiv:2111.03634  
Abbott, R., Abbott, T. D., Acernese, F., et al. 2021d, arXiv:2111.03606  
Abbott, R., Abbott, T. D., Abraham, S., et al. 2021e, *PhRvD*, 104, 022004  
Abbott, R., Abe, H., Acernese, F., et al. 2021, arXiv:2111.03604

Acernese, F., Agathos, M., Agatsuma, K., et al. 2015, *CQGra*, 32, 024001  
Acernese, F., Agathos, M., Aiello, L., et al. 2019, *PhRvL*, 123, 231108  
Adhikari, S., Fishbach, M., Holz, D. E., Wechsler, R. H., & Fang, Z. 2020, *ApJ*, 905, 21  
Aghanim, N., Akrami, Y., Ashdown, M., et al. 2020, *A&A*, 641, A6  
Akutsu, T., Ando, M., Arai, K., et al. 2019, *NatAs*, 3, 35  
Akutsu, T., Ando, M., Arai, K., et al. 2021, *PTEP*, 2021, 05A101  
Artale, M. C., Mapelli, M., Bouffanais, Y., et al. 2020, *MNRAS*, 491, 3419  
Artale, M. C., Mapelli, M., Giacobbo, N., et al. 2019, *MNRAS*, 487, 1675  
Astropy Collaboration, Robitaille, T. P., Tollerud, E. J., et al. 2013, *A&A*, 558, A33  
Banerjee, S., Baumgardt, H., & Kroupa, P. 2010, *MNRAS*, 402, 371  
Behroozi, P. S., Wechsler, R. H., & Conroy, C. 2013, *ApJL*, 762, L31  
Bocquet, S., & Carter, F. W. 2016, *JOSS*, 1, 46  
Cheng, Y.-T., Chang, T.-C., Bock, J., Bradford, C. M., & Cooray, A. 2016, *ApJ*, 832, 165  
Comparat, J., Zhu, G., Gonzalez-Perez, V., et al. 2016, *MNRAS*, 461, 1076  
Diaz, C. C., & Mukherjee, S. 2022, *MNRAS*, 511, 2782  
Dominik, M., Belczynski, K., Fryer, C., et al. 2012, *ApJ*, 759, 52  
Doré, O., Bock, J., Ashby, M., et al. 2014, arXiv:1412.4872  
Farr, B., Berry, C. P. L., Farr, W. M., et al. 2016, *ApJ*, 825, 116  
Favole, G., Gonzalez-Perez, V., Stoppacher, D., et al. 2020, *MNRAS*, 497, 5432  
Fishbach, M., Holz, D. E., & Farr, W. M. 2018, *ApJL*, 863, L41  
Fishbach, M., & Kalogera, V. 2021, *ApJL*, 914, L30  
Gong, Y., Chen, X., & Cooray, A. 2020, *ApJ*, 894, 152  
Gong, Y., Cooray, A., Silva, M. B., et al. 2017, *ApJ*, 835, 273  
Hall, E. D., & Evans, M. 2019, *CQGra*, 36, 225002  
Hunter, J. D. 2007, *CSE*, 9, 90  
Jones, E., Oliphant, T., Peterson, P., et al. 2001, SciPy: Open source scientific tools for Python, <http://www.scipy.org/>  
Kennicutt, R. C., Jr. 1998, *ARA&A*, 36, 189  
Kovetz, E. D., Viero, M. P., Lidz, A., et al. 2017, arXiv:1709.09066  
Lidz, A., & Taylor, J. 2016, *ApJ*, 825, 143  
Ly, C., Malkan, M. A., Kashikawa, N., et al. 2007, *ApJ*, 657, 738  
Madau, P., & Dickinson, M. 2014, *ARA&A*, 52, 415  
Madau, P., & Fragos, T. 2017, *ApJ*, 840, 39  
Mastrogiovanni, S., Leyde, K., Karathanasis, C., et al. 2021, *PhRvD*, 104, 062009  
McCarthy, K. S., Zheng, Z., & Ramirez-Ruiz, E. 2020, *MNRAS*, 499, 5220  
Moradinezhad Dizgah, A., Keating, G. K., Karkare, K. S., Crites, A., & Choudhury, S. R. 2022, *ApJ*, 926, 137  
Mukherjee, S., & Silk, J. 2021, *MNRAS*, 506, 3977  
Mukherjee, S., Wandelt, B. D., Nissanke, S. M., & Silvestri, A. 2021, *PhRvD*, 103, 043520  
O’Shaughnessy, R., Kalogera, V., & Belczynski, K. 2010, *ApJ*, 716, 615  
Punturo, M., Abernathy, M., Acernese, F., et al. 2010, *CQGra*, 27, 194002  
Safarzadeh, M., & Berger, E. 2019, *ApJL*, 878, L12  
Safarzadeh, M., Berger, E., Leja, J., & Speagle, J. S. 2019, *ApJL*, 878, L14  
Saito, S., de la Torre, S., Ilbert, O., et al. 2020, *MNRAS*, 494, 199  
Sathyaprakash, B. S., Schutz, B. F., & Van Den Broeck, C. 2010, *CQGra*, 27, 215006  
Scelfo, G., Spinelli, M., Raccanelli, A., et al. 2022, *JCAP*, 01, 004  
Silva, M. B., Santos, M. G., Cooray, A., & Gong, Y. 2015, *ApJ*, 806, 209  
Toffano, M., Mapelli, M., Giacobbo, N., Artale, M. C., & Ghirlanda, G. 2019, *MNRAS*, 489, 4622  
van der Walt, S., Colbert, S. C., & Varoquaux, G. 2011, *CSE*, 13, 22  
Vitale, S., Farr, W. M., Ng, K., & Rodriguez, C. L. 2019, *ApJL*, 886, L1  
Yang, S., & Lidz, A. 2020, *MNRAS*, 499, 3417